Bio-Design and Manufacturing (2023) 6:676–690
https://doi.org/10.1007/s42242-023-00245-3

RESEARCH ARTICLE

# Polyvinylpyrrolidone-based bioink: influence of bioink properties on printing performance and cell proliferation during inkjet-based bioprinting

Wei Long Ng[1,2] · Xi Huang[1] · Viktor Shkolnikov[3] · Ratima Suntornnond[1] · Wai Yee Yeong[1,2]

Received: 18 January 2023 / Accepted: 11 May 2023 / Published online: 30 August 2023


## Abstract

Among the different bioprinting techniques, the drop-on-demand (DOD) jetting-based bioprinting approach facilitates contactless deposition of pico/nanoliter droplets of materials and cells for optimal cell–matrix and cell–cell interactions. Although bioinks play a critical role in the bioprinting process, there is a poor understanding of the influence of bioink properties on printing performance (such as filament elongation, formation of satellite droplets, and droplet splashing) and cell health (cell viability and proliferation) during the DOD jetting-based bioprinting process. An inert polyvinylpyrrolidone (PVP360, molecular weight=360 kDa) polymer was used in this study to manipulate the physical properties of the bioinks and investigate the influence of bioink properties on printing performance and cell health. Our experimental results showed that a higher bioink viscoelasticity helps to stabilize droplet filaments before rupturing from the nozzle orifice. The highly stretched droplet filament resulted in the formation of highly aligned "satellite droplets," which minimized the displacement of the satellite droplets away from the predefined positions. Next, a significant increase in the bioink viscosity facilitated droplet deposition on the wetted substrate surface in the absence of splashing and significantly improved the accuracy of the deposited main droplet. Further analysis showed that cell-laden bioinks with higher viscosity exhibited higher measured average cell viability (%), as the presence of polymer within the printed droplets provides an additional cushioning effect (higher energy dissipation) for the encapsulated cells during droplet impact on the substrate surface, improves the measured average cell viability even at higher droplet impact velocity and retains the proliferation capability of the printed cells. Understanding the influence of bioink properties (e.g., bioink viscoelasticity and viscosity) on printing performance and cell proliferation is important for the formulation of new bioinks, and we have demonstrated precise DOD deposition of living cells and fabrication of tunable cell spheroids (nL–μL range) using multiple types of cells in a facile manner.

✉ Wei Long Ng
ng.wl@ntu.edu.sg

✉ Wai Yee Yeong
wyyeong@ntu.edu.sg

[1] HP-NTU Digital Manufacturing Corporate Lab, Nanyang Technological University (NTU), Singapore 637460, Singapore

[2] Singapore Centre for 3D Printing (SC3DP), School of Mechanical and Aerospace Engineering, Nanyang Technological University (NTU), Singapore 639798, Singapore

[3] HP Inc., Palo Alto, CA 94304, USA

**Graphic abstract**

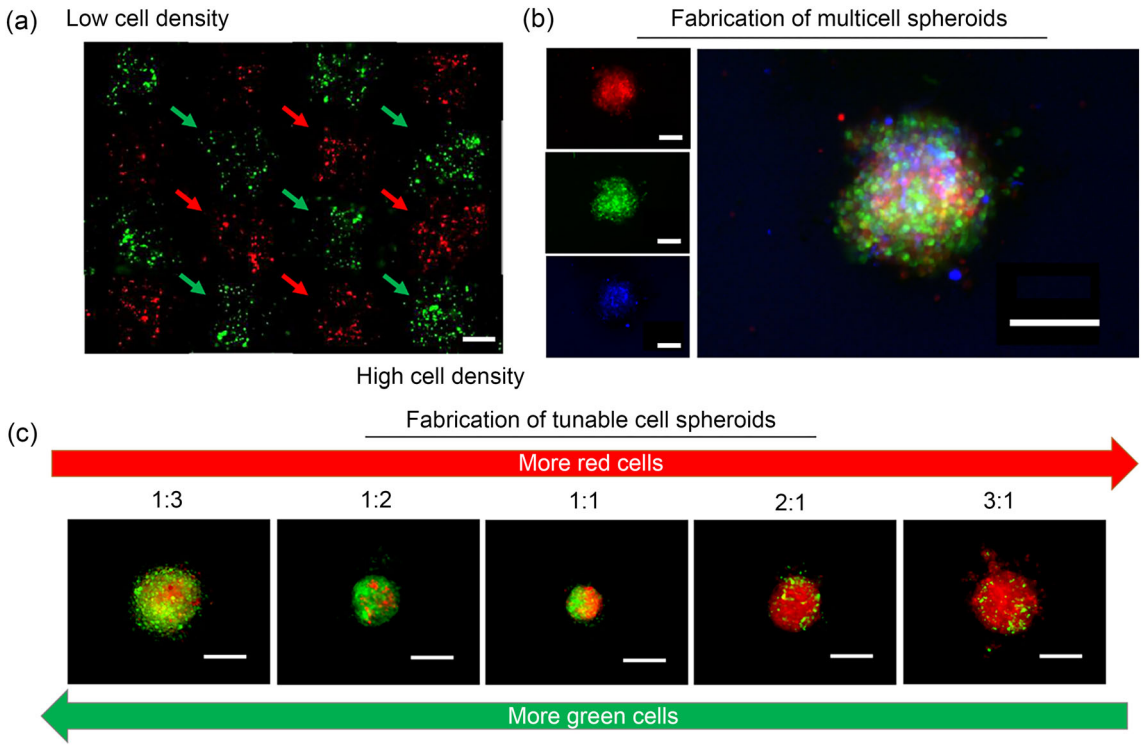


**Keywords** Biofabrication · 3D bioprinting · Drop-on-demand bioprinting · Bioink properties · Polyvinylpyrrolidone

## Introduction

Over the years, three-dimensional (3D) bioprinting systems have been commonly used for the deposition of highly viable cells during the bioprinting process to fabricate biomimetic 3D tissue-engineered constructs for tissue engineering, regenerative medicine, and biomedical applications [1–7]. 3D bioprinting technologies can be categorized into three distinct groups according to the American Society of Testing and Materials (ASTM) standards—jetting-based [8–11], extrusion-based [12–16], and vat polymerization-based [17–19] bioprinting. Each bioprinting technology has its specific advantages and limitations; and the selection of an appropriate bioprinting technology should be based on its intended application. The key advantages of each bioprinting technology are as follows: the jetting-based bioprinting approach facilitates contactless drop-on-demand (DOD) printing of different types of biomaterials and living cells on a two-dimensional (2D) planar surface to optimize cell–matrix and cell–cell interactions, the material extrusion bioprinting approach has higher throughput rates and a wider range of printable bioinks, and the vat polymerization bioprinting approach can achieve high printing resolution and high printable cell concentration.

Compared to the other 3D bioprinting approaches, the jetting-based bioprinting approach facilitates a higher degree of control over printed cell density by manipulating the number of printed cell-laden droplets at specific spots/regions [20, 21] and can be used to manipulate the spatial patterning of living cells and biomaterials for fundamental biological studies [22–24]. Contactless DOD jetting-based bioprinting approaches include inkjet bioprinting [25], microvalve bioprinting [26], acoustic bioprinting [27], and laser-assisted bioprinting [28]. Among these approaches, the thermal inkjet approach has the advantages of lower manufacturing cost and higher nozzle density, achieving a higher dispensing throughput [29]. Furthermore, previous studies have reported that the generated heat did not induce significant damage to printed cells during the thermal inkjet bioprinting process (80%–90% cell viability after printing) [29]. The printed cells in the jetting-based bioprinting approach are usually encapsulated within uncrosslinked bioinks of low viscosity (3–10 mPa·s) [30], and a limited range of hydrogel-based bioinks such as alginate [31–33], collagen-based [34–37],

gelatin-based [38–41], fibrin-based [42, 43] and polyethylene glycol (PEG) [44–46] can be printed at relatively low concentrations due to the stringent bioink requirements (bioink viscosity, surface tension and density) [47].

Although bioinks play a critical role in the bioprinting process, there is a poor understanding of the influence of bioink properties on printing performance and cell proliferation upon impact during contactless DOD jetting-based bioprinting processes. To the best of our knowledge, there are limited studies that have investigated the droplet formation process [48, 49] and shear stress-induced damage within nozzles [50, 51] for cell-laden bioinks in jetting-based bioprinting processes. In this work, a holistic approach was taken to analyze the influence of bioink properties on (1) the printing performance of deposited cell-laden droplets (droplet formation process, satellite droplet displacement, and droplet splashing process) and (2) cell viability upon impact on the substrate surface. Polyvinylpyrrolidone (PVP) is an inert and nontoxic polymer commonly used as an excipient in pharmaceuticals [52], and its low viscosity makes it a suitable polymer for jetting-based bioprinting applications [53–55]. An inert polyvinylpyrrolidone (PVP360, molecular weight=360 kDa) polymer was used in this study to manipulate the physical properties of the bioinks and evaluate the influence of bioink properties on printing performance and cell health in inkjet-based bioprinting.

Our study showed that a higher bioink viscoelasticity helps to stabilize the droplet filament. The highly stretched droplet filament ruptured from the nozzle orifice and formed highly aligned "satellite droplets," which followed closely behind the main primary droplet and improved the overall printing quality. Next, an increase in the bioink viscosity facilitated droplet deposition on the wetted substrate surface in the absence of splashing and significantly improved the accuracy of the deposited main droplet. Further analysis showed that cell-laden bioinks with higher viscosity exhibited higher measured average cell viability (%), as the presence of polymer within the printed droplets provides an additional cushioning effect (higher energy dissipation) for the encapsulated cells during droplet impact on the substrate surface, improves the measured average cell viability even at higher droplet impact velocity and retains the proliferation capability of the printed cells.

## Materials and methods

### Bioink synthesis

Different concentrations of PVP-based bioinks (PVP360 from Sigma Aldrich, Singapore, Singapore) were prepared and used in all experiments. Briefly, the PVP powder was first ultraviolet (UV)-sterilized for 60 min before solubilization in 0.0067 mol sterile, filtered 1×phosphate-buffered saline (PBS) solution HyClone™ without calcium ($Ca^{2+}$) and magnesium ($Mg^{2+}$) to obtain the desired 0–0.02 g/mL PVP-based bioinks. Mechanical stirring was performed for 5 min to break up the PVP clumps, followed by centrifugation at 500× *g* for 5 min at room temperature. This mechanical stirring and centrifugation process was repeated until a homogeneous PVP-based bioink was obtained.

### Bioink printability

A thermal inkjet printer (HP D300e Digital Dispenser, printing frequency up to 1 kHz) was used for cell patterning applications using non-commercial cell-printing prototype cassettes with eight embedded thermal inkjet print-heads with a large nozzle orifice diameter (80 μm). The thermal inkjet print-head facilitated droplet printing with a constant droplet volume of about 0.345 nL, and the desired volume at each specific spot could be controlled by manipulating the number of printed droplets. In this study, the HP D300e Digital Dispenser was used to evaluate the printing performance of different PVP-based bioinks (0–0.02 g/mL), and the nozzle-to-substrate distance was approximately 15 mm (which is equivalent to the thickness of the tissue-culture well plate).

### Bioink characterization

Various measurements were performed on the different PVP-based bioinks (0–0.02 g/mL) to evaluate the influence of polymer concentration on the physical properties of the bioinks (viscosity, surface tension, and density) and their respective *Z* values. A Discovery hybrid rheometer (TA Instruments, New Castle, DE, USA) was used to evaluate the rheological properties of the PVP-based bioinks. The strain amplitudes of the various bioinks were determined, and subsequent measurements were performed within the measured linear viscoelastic region. The viscosities of different PVP-based bioinks were evaluated for shear rates ranging from $1\times10^2$ to $1\times10^4$ $s^{-1}$ at a constant temperature of 25 °C. The surface tension of the PVP-based under Bioink characterization, the optical contact angle system (OCA 15 EC, Data Physics Instrument, Filderstadt, Germany), and a weighing balance was used to measure the density of the PVP-based bioinks (weight per mL of bioink). A Zetasizer Nano ZS (Malvern Panalytical, United Kingdom) was used to determine the hydrodynamic radius of the PVP polymer at different concentrations using dynamic light scattering; the material refractive index was 1.525 with a material absorption value of 0.016, the dispersant viscosity was 0.8882 mPa s and the dispersant refractive index was 1.33. A sample size of 3 was used for all the measurements. The measured viscosity, surface tension and density of the PVP-based bioinks were then used

to determine the bioink printability using the dimensionless $Z$ value—the inverse of the Ohnesorge number ($Oh$), which can be defined as the ratio between the Reynolds number and the square root of the Weber number and is independent of the bioink velocity.

## High-speed droplet imaging

A high-speed camera (Photron Nova S12, up to 200,000 frames per second) and an objective lens (Canon MP-E 65 mm f/2.8 1–5× Macro lens) were used to capture high-speed images of cell-laden droplets as they travelled from the nozzle and impacted the substrate surface (about 15 mm distance).

### Droplet formation analysis

High-speed images were captured at 100,000 frames per second, 1× zoom and 1/950,000 shutter speed during the droplet printing process to obtain the full profile of the droplets travelling along the nozzle–substrate distance of about 15 mm. The captured high-speed images for the different PVP-based bioinks were used to determine the maximum droplet elongation, droplet rupture time, droplet velocity profile, number of satellite droplets, and satellite droplet displacement. The average droplet velocity profile can be obtained by calculating the distance travelled by the droplets ($n$=15) between subsequent frames (10 μs apart).

### Droplet splashing analysis

The impact of the droplet on the substrate was recorded at 144,000 frames per second, 5× zoom and 1/950,000 shutter speed. The captured high-speed images near the substrate surface were used to determine the influence of the polymer concentration on the droplet impact velocity and main droplet displacement.

## Cell printing

Primary human dermal fibroblasts (HDFs) used in this study (between Passages 3–5) were purchased from CellnTec Advanced Cell Systems. The recommended CnT-Prime Fibroblast Proliferation Medium (CnT-PR-F, 0.01 g/mL serum medium supplemented with fully defined growth factors and cofactors) was used to culture the fibroblasts at a temperature of 37 °C and 5% $CO_2$, and the culture medium was changed every three days. The adherent fibroblasts were harvested at 90% confluency using CnT Accutase cell detachment solution (CnT-Accutase 100). To understand the influence of polymer concentration on the bioprinting process, detached fibroblasts were suspended in different PVP-based bioinks (0 and 0.02 g/mL) to obtain different concentrations of cell-laden bioinks (0–$3\times10^6$ cells/mL). The PBS solution was used in this study as a control baseline to understand the influence of polymer concentration on droplet impact velocity and its corresponding cell viability.

To further demonstrate the long-term proliferation profile of the printed cells, primary human dermal fibroblasts were printed using the optimal bioink with the highest cell viability and cultured over a period of seven days inside an incubator. The PrestoBlue® assay was used to measure the proliferation profile of printed cells based on the normalized relative fluorescence units (RFUs) over a period of seven days (Days 1, 3, and 7) post printing. Fresh culture medium was added to cells prior to the addition of the PrestoBlue® assay (10% of the total volume) at a volume ratio of 9:1, followed by incubation at 37 °C for 2 h. A microplate reader was then used to excite the PrestoBlue® assay at 560 nm wavelength and measure its fluorescence emission at 590 nm wavelength. The measured fluorescence units for the different fluorescence measurements were then normalized to the control group at Day 1 to obtain the normalized RFUs for easy comparison.

## Cell patterning

For cell patterning application, the HDFs were stained separately using green and orange cytoplasmic membrane dyes (CellBrite®, Biotium) and suspended in 2% (0.02 g/mL) PVP-based bioinks to obtain stained cells at a final concentration of $3\times10^6$ cells/mL. The printed cell density on a planar surface can be controlled by printing varying numbers of cell-laden droplets at each predefined location.

For fabrication of multicell spheroids and tunable cell spheroids, the HDFs were stained separately using green, orange, and blue cytoplasmic membrane dyes (CellBrite®, Biotium) and suspended in 2% PVP-based bioinks to obtain stained cells at a final concentration of $3\times10^6$ cells/mL. A thermal inkjet printer (HP D300e Digital Dispenser) was used to dispense cell-laden droplets into 96-well round bottom plates (Thermo Fisher™ Nunc MicroWell Plates) that were filled with 200 μL of cell culture medium. The cell-laden droplets were printed at 1 kHz into 96-well round bottom plates at different volume ratios to fabricate cell spheroids (total volume=2400 nL). The printed cell-laden droplets were immediately incubated at 37 °C with 5% $CO_2$ supply for a week before observation under a fluorescence microscope (Axio Vert. A1, Carl Zeiss, Germany).

## Statistical analysis

Statistical analysis was performed using the raw data, and all experimental results are presented as the mean±standard deviation. One-way analysis of variance (ANOVA) and Tukey's honestly significant difference (HSD) test were used

to determine the significance of differences between pairs or group means. Significance levels are as follows: $^{***}p<0.001$ as the most significant and $^{*}p<0.05$ as the least significant.

## Results and discussion

### Droplet formation analysis

The printability in a thermal inkjet bioprinting system is highly dependent on the physical properties of bioinks (viscosity, surface tension and density) to successfully eject discrete droplets onto an underlying substrate in a contactless manner, and it can be expressed in terms of the dimensionless $Z$ number:

$$Z = \frac{Re}{(We)^{1/2}} = \frac{(r\rho\gamma)^{1/2}}{\eta}, \tag{1}$$

where

$$Re = \frac{vr\rho}{\eta}, \tag{2}$$

$$We = \frac{v^2 r\rho}{\gamma}. \tag{3}$$

$Re$ is Reynolds number, and $We$ is Weber number. The other parameters include $v$, $\rho$, $\eta$, and $\gamma$ which represent the average droplet velocity, density, viscosity, and surface tension of the bioinks respectively, and $r$ is a characteristic dimension (radius of the nozzle orifice).

It has been reported that a range of $1<Z<14$ is optimal for discrete droplet printing; there is too much viscous dissipation for droplet formation when $Z<1$, and there is a high tendency for satellite droplet formation when $Z>14$ [56]. In this study, we evaluated the influence of PVP polymer concentration on the physical properties of bioinks and its effect on droplet formation. Generally, the measured viscosity and density of the PVP-based bioinks increase with increasing polymer concentration, whereas the surface tension of the PVP-based bioinks decreases with increasing polymer concentration. Notably, the change in bioink viscosity is more significant than the change in surface tension and density with increasing polymer concentration. We measured the ink viscosity as a function of shear rate for shear rates of 100–10,000 $s^{-1}$. We observed that in the measured range, the viscosity followed the Ostwald–de Waele power law,

$$\eta = K(T)\dot{\gamma}^{n-1}, \tag{4}$$

where $\eta$ is the apparent viscosity, $\dot{\gamma}$ is the shear rate, $K(T)$ is the temperature-dependent flow consistency index, and $n$ is the flow behaviour index. For our solutions, we estimated $K(T)$ to be 0.7717, 3.1921, and 5.6457, and $n$ to be 0.987, 0.986, and 0.990 for 0%, 1% (0.01 g/mL), and 2% (0.02 g/mL) PVP solutions, respectively. In our experiments, the relevant shear rate scales with the ratio of the drop initial velocity (about 20 m/s) to the drop radius (40 μm) and is on the order of 500,000 $s^{-1}$. Since our viscometer (and most common viscometers) can only measure at shear rates of up to 10,000 $s^{-1}$, we used the Ostwald–de Waele power law to extrapolate the viscosity to our experimentally relevant shear rate. The measured viscosity values at 10,000 $s^{-1}$ were 0.687, 2.793, and 5.177 mPa·s, while the Ostwald–de Waele extrapolated viscosities at 500,000 $s^{-1}$ were 0.651, 2.656, and 4.951 mPa·s, respectively (Fig. 1a). The measured average density values were 1006.6, 1015.2, and 1026.5 kg/$m^3$, and the surface tension values were 72.1, 59.1, and 56.4 mN/m (Fig. 1b) for 0%, 1%, and 2% PVP, respectively.

The physical properties (viscosity, surface tension and density) of different cell-laden bioinks were used to calculate the dimensionless $Z$ value, which can be used to predict the printability of a bioink. Overall, increasing the PVP concentration resulted in lower dimensionless $Z$ numbers—82.82, 18.44, and 9.72 for 0%, 1%, and 2% PVP, respectively (Fig. 1c).

During the inkjet bioprinting process, the liquid in the nozzle was first accelerated and ejected out of the nozzle orifice. The meniscus quickly extended outwards until a liquid column with a round leading edge was formed; the decrease in the liquid flow rate from the nozzle resulted in a difference in the axial velocity between the column head and the liquid at the nozzle orifice, which induced stretching of the liquid column (droplet filament elongation). Next, a negative velocity pulse (pull-back) pulled the liquid tail back to induce rapid thinning. The liquid tail at the nozzle orifice necked, and the radius of the liquid thread decreased rapidly until it eventually pinched off from the nozzle orifice [57]. There was no significant droplet filament elongation without the presence of PVP polymer, and unstable droplet formation was observed. Numerous small satellite droplets were observed behind the main primary droplet upon ejection for the 0% PVP-based bioink ($Z$=78.45) (Fig. 1d). This phenomenon is corroborated by previous studies that showed that if the polymer relaxation time is greater than the inertial-capillary break-up time, then shear thinning polymer additives can stabilize the jet [58], while high dimensionless $Z$ numbers result in the formation of undesirable satellite droplets during inkjet printing [56]. That is, polymer additives are stabilizing if

$$\frac{2\pi\mu z_0^3}{kT}\left(\frac{\gamma_{LV}}{\rho d^3}\right)^{1/2} > 1, \tag{5}$$

where $\mu$ is the shear viscosity of the solution, $z_0$ is the equilibrium size of the coiled macromolecule (here taken as the radius of gyration), $k$ is Boltzmann's constant, $T$ is the absolute temperature, $\gamma_{LV}$ is the liquid-vapour surface tension

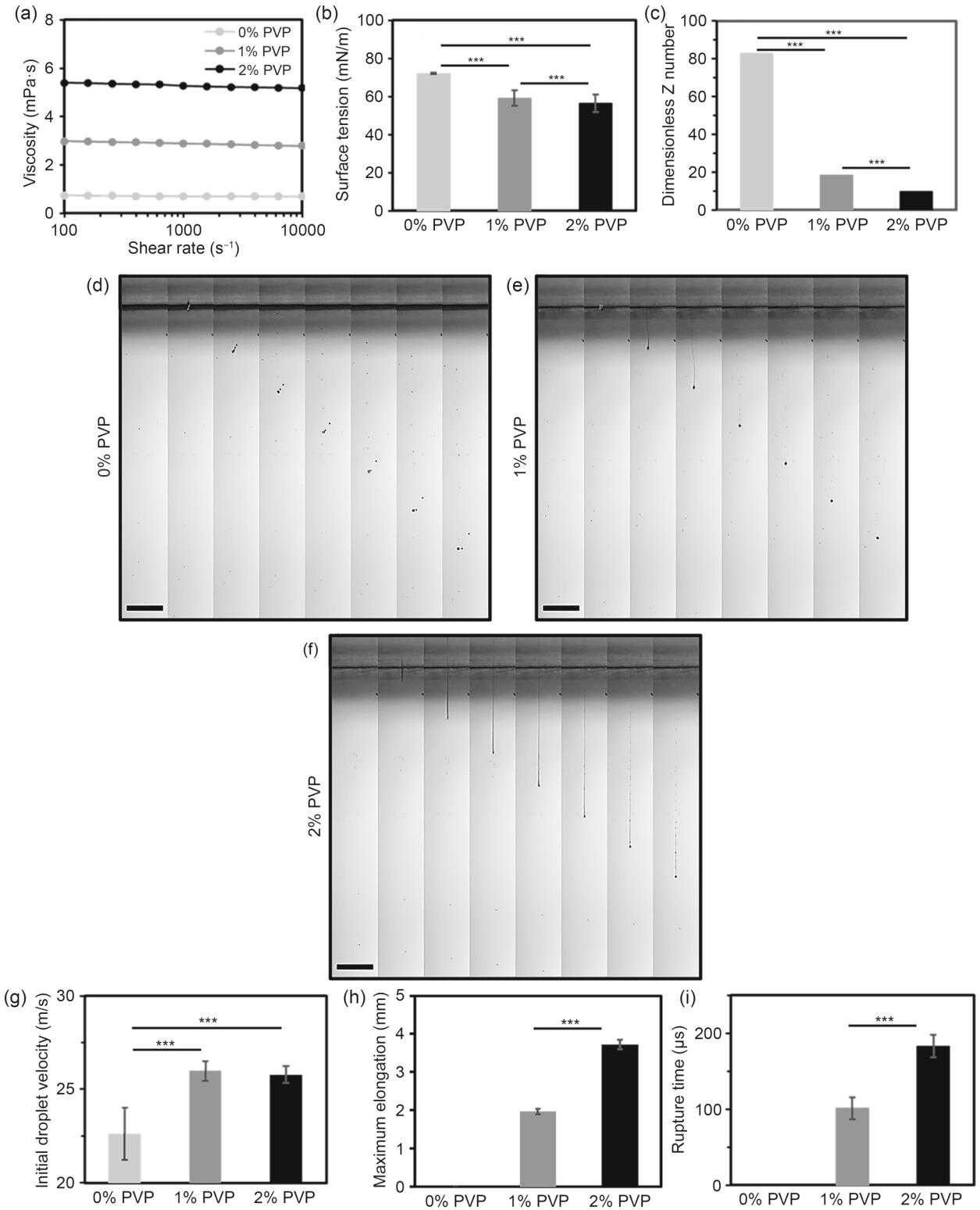


**Fig. 1** **a–c** Measurement of viscosity, surface tension and its corresponding dimensionless *Z* number, which can be used as indicators for bioink printability, with a sample size of three. **d–f** Representative images of droplet formation for different (0%, 1%, and 2%) PVP-based bioinks near the nozzle orifice were captured at 100,000 frames per second, and the images were stacked at 4 frames apart (25,000 frames per second, 40 μs apart, scale bar=1 mm). **g** The average initial droplet velocity near the nozzle orifice, **h** resultant maximum droplet elongation before rupturing from the nozzle orifice, and **i** rupture time, which represents the duration before the elongated filament detaches from the nozzle orifice. Data are represented as mean±standard deviation, n = 15, ***p < 0.001. PVP: polyvinylpyrrolidone; 1% PVP: 0.01 g/mL PVP; 2% PVP: 0.02 g/mL PVP

measured at the fluid-air interface, $\rho$ is the density, and $d$ is the diameter of the nozzle orifice. To obtain the radius of gyration, we measured the hydrodynamic radius using dynamic light scattering and then inferred the radius of gyration via the experimental correlation, where $z_0 = 1.3z_h$ (with $z_h$ being the hydrodynamic radius) [59]. For 1% and 2% PVP, we obtained radii of gyration of 35 and 23 nm, respectively. The calculated ratios of polymer relaxation time to inertial-capillary break time for both 1% and 2% PVP were greater than 1, suggesting that PVP should stabilize filament elongation at these concentrations. When polymer additives stabilize the filament, the breakup time is dominated by the polymer relaxation time, $t_r$:

$$t_r = \frac{2\pi\mu z_0^3}{kT}. \tag{6}$$

Significant droplet filament elongation was observed for both 1% and 2% PVP-based bioinks, and the degree of droplet filament elongation increased with increasing PVP polymer concentration before rupturing from the nozzle orifice (Figs. 1e and 1f, and Fig. S1 in Supplementary Information). We attribute this to the elastic stresses in the PVP-laden filament preventing it from disintegration [58]. An analysis of the droplet velocity using the high-speed images showed that the presence of PVP polymer resulted in a significantly higher initial droplet velocity when ejected from the nozzle orifice; the initial drop velocity increased from (22.64±1.39) m/s for the 0% PVP-based bioink to (25.98±0.53) m/s and (25.79±0.44) m/s for the 1% and 2% PVP-based bioinks, respectively (Fig. 1g). An increase in polymer concentration resulted in longer filament elongation from (1.97±0.07) mm (aspect ratio of 24.6) for the 1% PVP-based bioink to (3.72±0.13) mm (aspect ratio of 46.5) for the 2% PVP-based bioink (Fig. 1h). The observed rupture time was (101±14.5) μs and (183±14.5) μs for the 1% and 2% PVP-based bioinks, respectively (Fig. 1i). As the nozzle is embedded 1 mm above the opening, the elongated droplets can only be observed by the high-speed camera about 38.5 μs after ejection using an initial drop velocity of about 26 m/s for both 1% and 2% PVP-based bioinks. Hence, the total rupture time was about 140 and about 220 μs for the 1% and 2% PVP-based bioinks, respectively. The rupture time was significantly faster than the firing frequency of the thermal inkjet print-head at 1 kHz (droplet firing interval=1000 μs); hence, the droplet filament elongation process did not interfere with the printing process. The observations were supported by earlier studies where dispensing higher polymer concentration solutions in HP thermal inkjet print-heads resulted in longer droplet filament elongation and a reduction in satellite droplet formation [58]. This observation was also confirmed in a more recent study, where a higher polymer concentration resulted in increasing viscoelastic behaviour of the fluid despite polymer chain extension at the pinch point, and both droplet filament elongation and rupture time increased with increased elasticity of the solution (Fig. S2 in Supplementary Information) [60].

The formation of satellite droplets during the inkjet printing process is considered undesirable because it affects the printing quality. As discussed in the previous section, an optimal range of dimensionless $Z$ numbers that vary between 1 and 14 is recommended for discrete droplet printing without the formation of satellite droplets. The typical diameter of a main primary droplet is similar to that of the nozzle orifice, whereas the diameter of satellite droplets is usually about 0.5–1 order of magnitude smaller than that of the main primary droplet. Apart from the size difference, there is a velocity difference between the main primary and satellite droplets. The larger satellite droplets (typically formed at the head of the filament tail) have higher velocity than the main primary droplet and merge with it before hitting the underlying substrate surface. On the other hand, the smaller satellite droplets (typically formed at the end of the filament tail) have lower momentum and are more likely to be blown away from the ejection axis by the lateral airflow [61].

Numerous small satellite droplets were observed upon ejection for the 0% PVP-based bioink ($Z$=82.82), and these small satellite droplets were randomly scattered behind the main primary droplet (Fig. 2a). In contrast, the addition of PVP polymer in both 1% PVP-based bioink ($Z$=18.44) and 2% PVP-based bioink ($Z$=9.72) suppressed the formation of satellite droplets during the initial droplet pinch-off from the nozzle orifice. The presence of the PVP polymer resulted in the formation of highly stretched filaments and initiated filament thinning during the droplet formation process. The thin PVP filament eventually broke up, and various pinch-off points occurred along the highly stretched filament to form numerous satellite droplets due to Rayleigh instability (Fig. 2d). Notably, a higher PVP concentration resulted in a highly stretched filament (up to an aspect ratio of 46.5), which broke apart to form numerous satellite droplets that followed closely behind the main primary droplet across the nozzle–substrate distance.

An analysis of the number of satellite droplets using the high-speed images showed that the presence of PVP polymer increased the number of formed satellite droplets (Fig. 2b). The number of satellite droplets observed in this study was 9.5±2.3, 11.3±2.2, and 14.1±3.1 for 0%, 1%, and 2% PVP-based bioinks, respectively (Fig. 2b). Although the presence of a higher PVP concentration induced the formation of more satellite droplets, the highly aligned satellite droplets followed closely behind the main primary droplet when the highly stretched PVP filament broke apart. An analysis of the corresponding satellite droplet displacement using the high-speed images showed a significant improvement in the

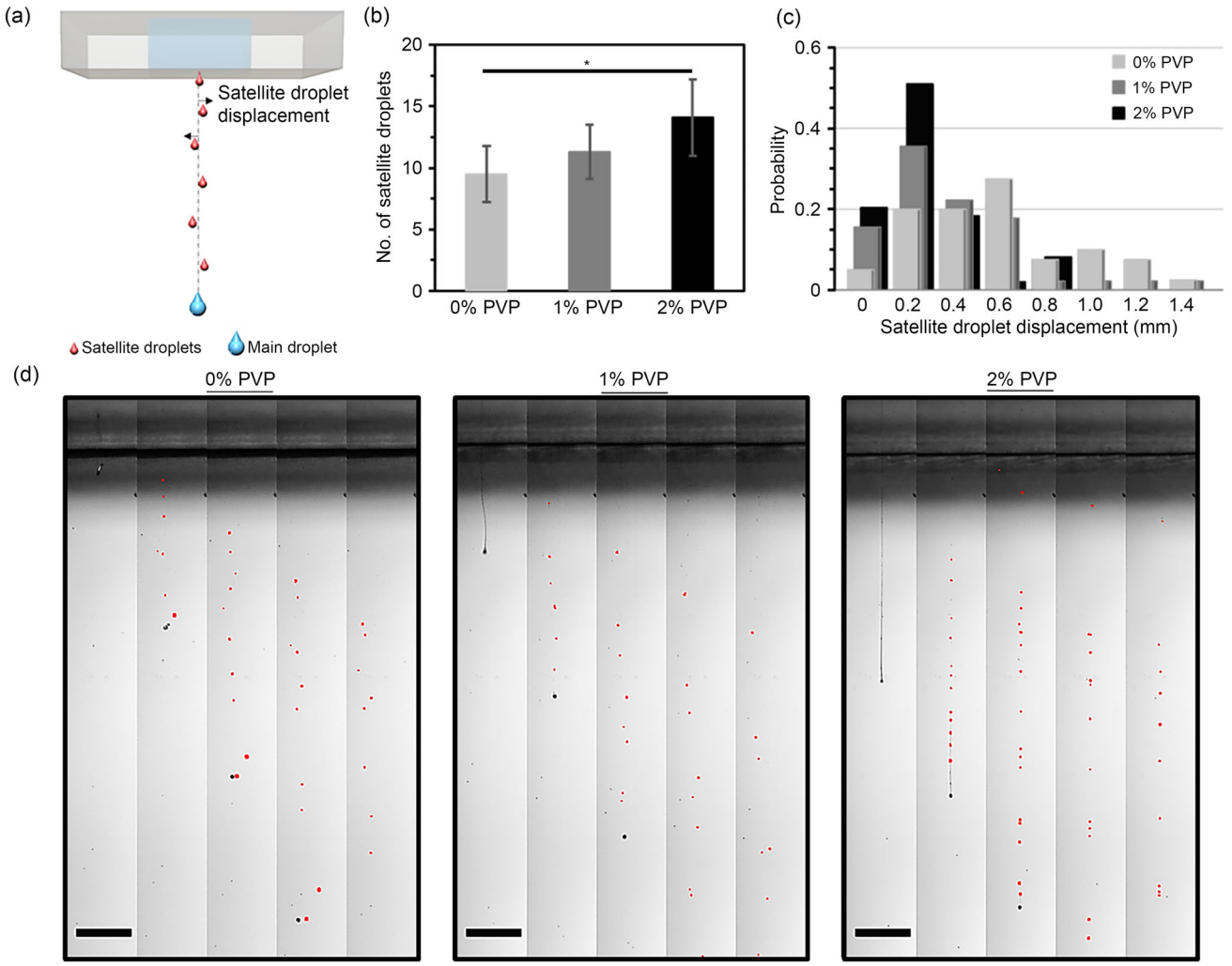


**Fig. 2** **a** Schematic drawing of the DOD bioprinting process to show the satellite droplet displacement using the main droplet as the reference. **b** Analysis of the number of satellite droplets using high-speed images. Data are represented as mean±standard deviation, n = 15, *p < 0.05. **c** Analysis of the satellite droplet displacement during the printing process (using 90 printed main droplets as reference). **d** Representative images showing the number of satellite droplets (highlighted in red) after rupturing from the nozzle orifice for different (0%, 1%, and 2%) PVP-based bioinks; images were 100 μs apart, scale bar=1 mm. DOD: drop-on-demand; PVP: polyvinylpyrrolidone; 1% PVP: 0.01 g/mL PVP; 2% PVP: 0.02 g/mL PVP

satellite droplet displacement at higher PVP polymer concentrations; the percentage of total satellite droplets within 0.2 mm displacement improved from 25.0% (0% PVP) to 51.1% (1% PVP) and 71.4% (2% PVP) (Fig. 2c and Fig. S3 in Supplementary Information). Hence, a higher PVP polymer concentration can potentially improve the overall printing quality by minimizing the displacement of undesirable satellite positions away from the predefined positions.

## Droplet splashing analysis

The printing quality during the inkjet printing process is dependent on two key factors: the accuracy of the deposited droplets on the substrate surface and the occurrence of droplet splashing [25, 62]. Hence, further analysis was performed to evaluate the influence of PVP polymer concentration on droplet deposition accuracy on the substrate surface and droplet splashing. During the DOD thermal printing process, multiple droplets were dispensed on the same spot at a constant droplet volume of about 0.345 nL to achieve the defined droplet volume. Consecutive droplet dispensing at the predefined location on the substrate surface resulted in surface wetting and formed a thin layer of liquid film, which transformed the dynamics to droplet impact on thin liquid films. There are several potential outcomes when a droplet hits a substrate surface, and these outcomes can be classified as (1) deposition, (2) prompt splash, and (3) corona splash. Droplet

deposition is characterized by the absence of splashing (without any break-up) upon droplet impact [63, 64]. In contrast, prompt splash induces the formation of small droplets during the advancement of lamella immediately after impact [62, 64], whereas corona splash exhibits clearly levitated lamellae that form a corona shape (bowl-like structure) that destabilizes and ejects multiple small droplets [62, 64]. It has been reported that a small air bubble will be entrapped under the centre of a deposited droplet on a dry substrate surface under atmospheric conditions, the lubrication pressure in the thin air layer is strong enough to facilitate deposition of subnanolitre droplets on a nonwetted surface [62], and deposition of different (0%, 1%, and 2%) PVP-based bioinks without splashing was observed on a dry substrate surface.

Repeated droplet dispensing on the predefined spot quickly wets the substrate surface to form a thin, continuous liquid film that transforms the dynamics to droplet impact on thin liquid films. Notably, droplet splashing will only occur when the ink properties and the process parameters exceed a threshold value, which is known as the splashing parameter, $K$ [65]. The splashing parameter is related to several dimensionless numbers, such as the Reynolds number $Re = \rho V_i D_0/\mu$, Weber number $We = \rho V_i^2 D_0/\gamma_{LV}$, and Ohnesorge number $Oh = We^{0.5}/Re$, where $D_0$ is the initial droplet diameter prior to impact, $V_i$ is the droplet's impact velocity, and $\rho$, $\mu$, and $\gamma_{LV}$ are the density, viscosity, and surface tension of the droplet liquid. There are many variants of this splashing parameter for different boundary conditions [66], and the splashing parameter for this study can be expressed in the form of

$$A \cdot Oh^a \cdot We^b = K_c, \tag{7}$$

where $A$, $a$, and $b$ are constants that are dependent on the boundary condition, and $K_c$ is the splashing parameter. The droplet will splash when $K_c$ is exceeded. In this variant, the condition for droplet impact upon a thin liquid film is similar to our printing condition, and the constants $a$ and $b$ were obtained from the best fit line using experimental data to obtain Eq. (1) [67]:

$$We = Oh^2 \cdot Re^2, \tag{8}$$

$$Oh \cdot Re^{1.17} = 63. \tag{9}$$

In particular, it should be noted that the above equations only provide qualitative information on whether splashing occurs and cannot provide insight into the magnitude of splashing. The measured droplet impact velocities were (20.21±0.29) m/s (0% PVP), (22.05±0.59) m/s (1% PVP), and (17.22±0.33) m/s (2% PVP) (Fig. 3a). The $Re$ values were 2368.93 (0% PVP), 641.09 (1% PVP) and 273.22 (2% PVP), the $We$ values were 456.18 (0% PVP), 667.95 (1% PVP) and 431.97 (2% PVP), and the corresponding $Oh$ values were $9.016\times10^{-3}$ (0% PVP), $4.031\times10^{-2}$ (1% PVP) and $7.607\times10^{-2}$ (2% PVP). The significant change in bioink viscosity with increasing PVP polymer concentration resulted in significantly lower $Re$ and larger $Oh$ values. The calculated $Oh \cdot Re^{1.17}$ values for different PVP-based bioinks in this study were 80.76 (0% PVP), 78.2 (1% PVP) and 54.4 (2% PVP), and splashing occurred for both 0% and 1% PVP-based bioinks (Fig. 3b).

The captured high-speed images near the substrate surface showed that both 0% and 1% PVP bioinks exhibited corona splashing (whereby the levitated lamella destabilized and ejected multiple small droplets), while the 2% PVP bioink resulted in droplet deposition on the wetted substrate surface (Fig. 3c). The 0% PVP-based bioink showed a slower droplet impact velocity ((20.21±0.29) m/s) than the 1% PVP-based bioink ((22.05±0.59) m/s); one possible reason is due to the continuous droplet rotation for the 0% PVP-based bioink while travelling from the nozzle orifice towards the substrate surface (Fig. 1d). Although the 1% PVP-based bioink exhibited a higher droplet impact velocity than the 0% PVP-based bioink, the presence of PVP polymer helped to mitigate the magnitude of corona splashing and reduce the number of ejected small droplets during splashing. Furthermore, an increase in the PVP polymer concentration resulted in a significantly slower droplet impact velocity from (22.05±0.59) m/s for 1% PVP to (17.22±0.33) m/s for 2% PVP. A slower droplet impact velocity and higher bioink viscosity in the 2% PVP-based bioink resulted in droplet deposition with the absence of splashing when the ejected main droplet landed on the wetted substrate surface. The observations in this work were similar to earlier reported studies on droplet impact dynamics [63]. There was a significant improvement in the main droplet displacement at higher PVP polymer concentrations; the percentage of total main droplets within 0.1 mm displacement improved from 48.9% (0% PVP) to 50.0% (1% PVP) and 90.0% (2% PVP) (Fig. 3d). Hence, the use of bioinks with higher viscosity helped to facilitate droplet deposition on the wetted substrate surface in the absence of splashing and significantly improved the accuracy of the deposited main droplet on the surface.

## Cell printing

The droplet impact velocity not only affects the droplet impact dynamics but also has a significant effect on the viability of printed cells. Analysis of the high-speed images showed that the measured droplet impact velocity generally decreases with increasing cell concentration, which is supported by other previous studies [49, 68]. An increase in cell concentration leads to higher viscous dissipation during the droplet formation process; hence, it results in a lower initial droplet velocity and droplet impact velocity at higher cell concentrations. Furthermore, the presence of PVP polymer

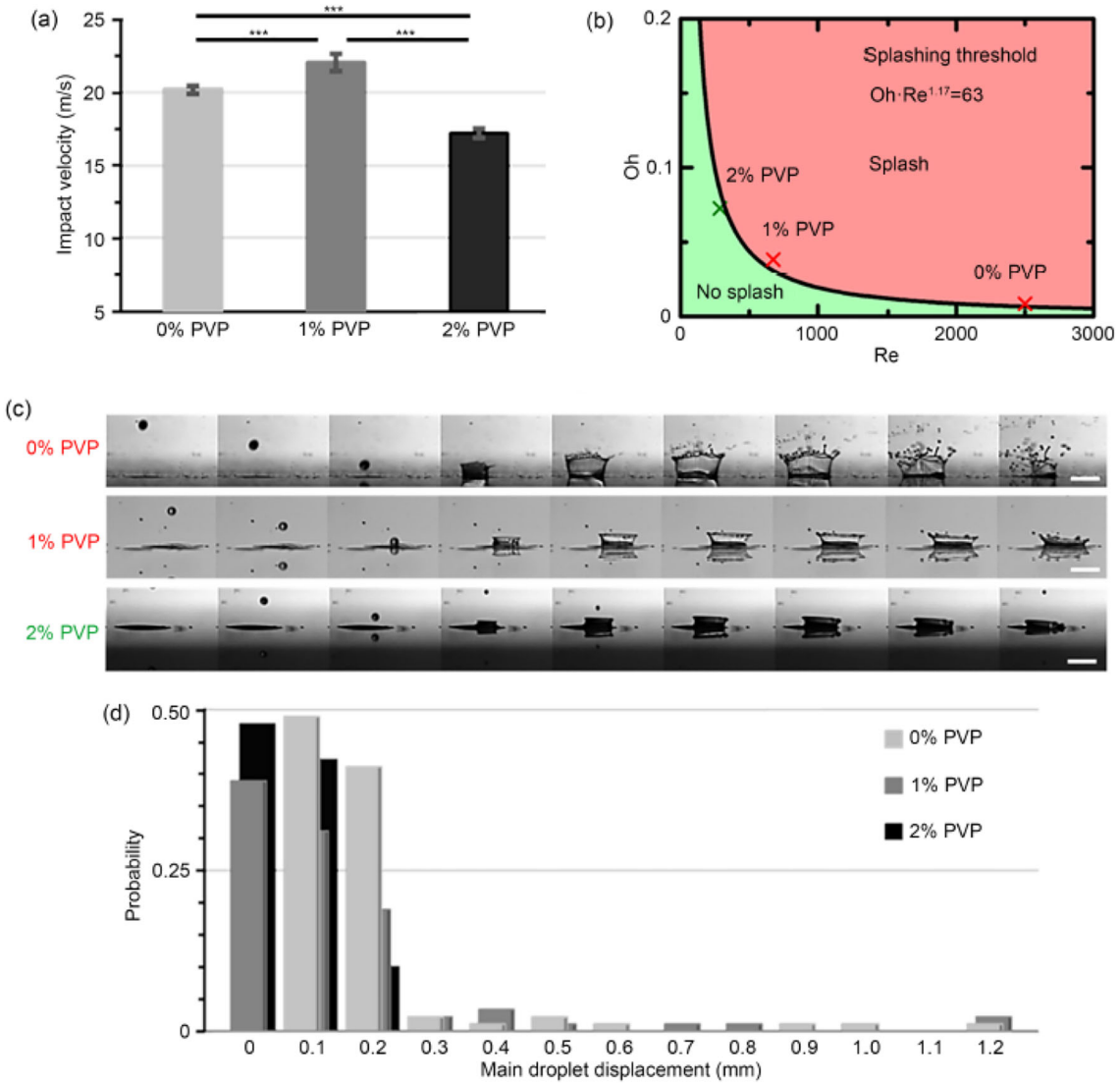


**Fig. 3** **a** Measured droplet impact velocity (0%, 1%, and 2% PVP-based bioinks) using high-speed images just before hitting the underlying substrate surface. Data are represented as mean±standard deviation, n = 15, ***$p < 0.001$. **b** Phase diagram of droplet splashing phenomenon computed using the splashing boundary conditions. **c** Representative high-speed images of ejected droplets (0%, 1%, and 2% PVP-based bioinks) travelling towards the underlying substrate surface at 5× zoom and 144,000 frames per second, scale bar=250 μm. **d** Analysis of the main droplet displacement during the printing process using 90 printed main droplets. PVP: polyvinylpyrrolidone

resulted in significantly higher droplet impact velocity at all cell concentrations ($1\times10^6$, $2\times10^6$, and $3\times10^6$ cells/mL). The measured droplet impact velocity for the 0% PVP-based bioink decreased from (14.27±0.33) m/s ($1\times10^6$ cells/mL) to (11.98±0.63) m/s ($2\times10^6$ cells/mL) and (10.11±0.88) m/s ($3\times10^6$ cells/mL), while the measured droplet impact velocity for the 2% PVP-based bioink decreased from (22.18±0.29) m/s ($1\times10^6$ cells/mL) to (18.54±0.33) m/s ($2\times10^6$ cells/mL) and (17.39±0.46) m/s ($3\times10^6$ cells/mL) (Fig. 4a).

The measured average cell viability (%) of printed cells using the live/dead cell viability assay showed an increase in cell viability (%) with increasing cell concentration (slower droplet impact velocity) and higher bioink viscosity; the viability of printed cells for the 0% PVP-based bioink increased from (69.32±8.18)% ($1\times10^6$ cells/mL) to (73.71±4.45)% ($2\times10^6$ cells/mL) and (84.00±5.10)% ($3\times10^6$ cells/mL), while the viability of printed cells for the 2% PVP-based bioink increased from (75.58±1.84)% ($1\times10^6$ cells/mL) to (85.33±2.70)% ($2\times10^6$ cells/mL) and (85.93±2.08)% ($3\times10^6$ cells/mL). The presence of PVP polymer within the printed droplets provides an additional cushioning effect (higher energy dissipation) for the encapsulated cells during droplet impact on the substrate surface and improves

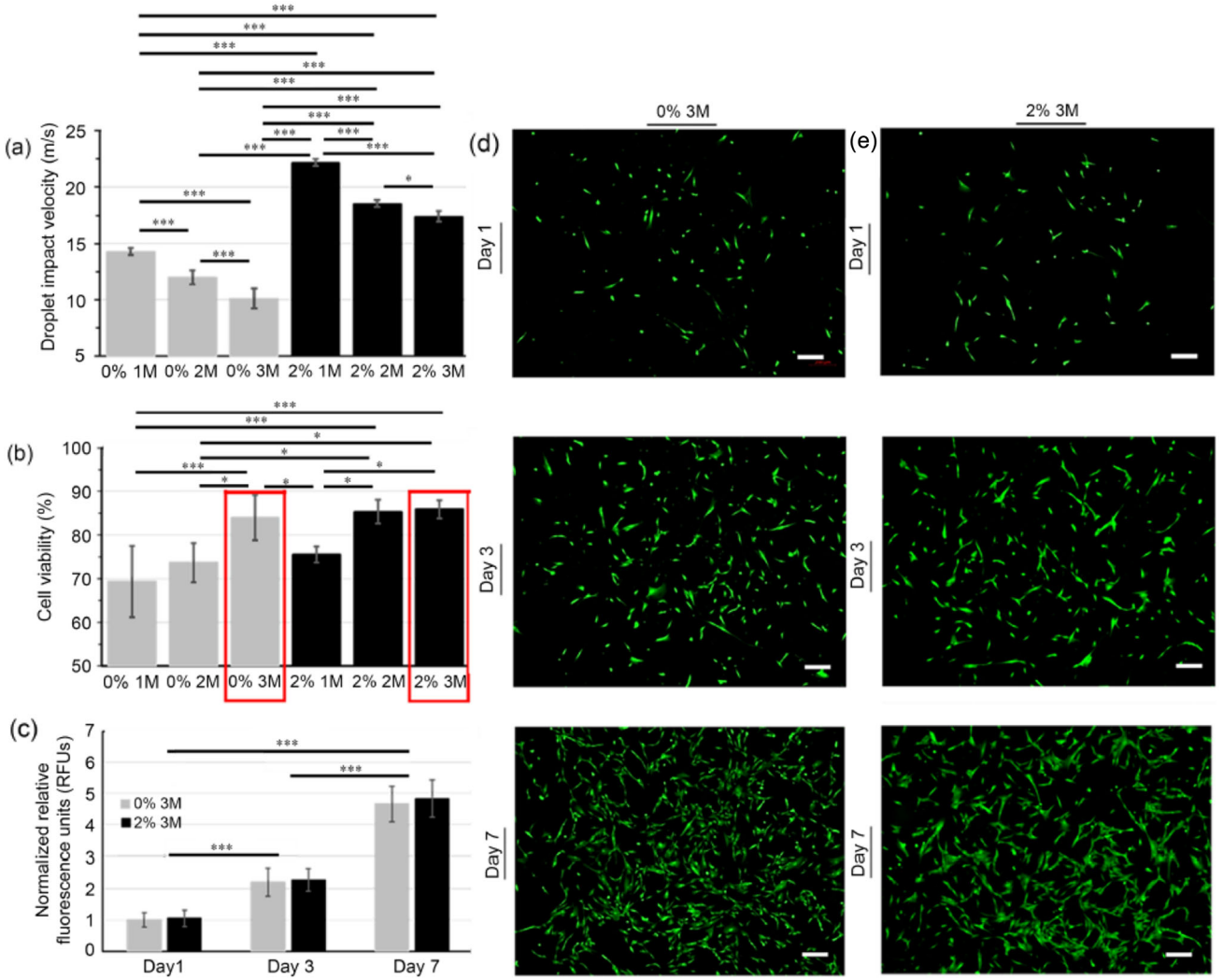


**Fig. 4** **a** Influence of cell concentrations ($1\times10^6$, $2\times10^6$, and $3\times10^6$ cells/mL) on droplet impact velocity for 0% and 2% PVP-based bioinks. **b** The corresponding cell viability (%) immediately after printing at different cell concentrations ($1\times10^6$, $2\times10^6$, and $3\times10^6$ cells/mL) for 0% and 2% PVP-based bioinks. **c** Analysis of the cell proliferation profile of 0% and 2% PVP-based bioinks using normalized RFUs from the PrestoBlue® assay at different time intervals (Days 1, 3 and 7). Data are represented as mean±standard deviation, n=15, *$p<0.05$, ***$p<0.001$. **d**, **e** Representative fluorescence images of the printed primary human dermal fibroblasts ($3\times10^6$ cells/mL) using live/dead cell viability assay in 0% and 2% PVP-based bioinks at 30 nL droplet volume per spot over a period of seven days, scale bar=200 μm. PVP: polyvinylpyrrolidone; 1 M: $1\times10^6$ cells/mL; 2 M: $2\times10^6$ cells/mL; 3 M: $3\times10^6$ cells/mL

the measured average cell viability even at higher droplet impact velocities (Fig. 4b). It is likely that the increased viscoelasticity of PVP solutions decreased the cell deformation during droplet impact. A previous study proposed that cell viability is a function of cell deformation; thus, decreasing cell deformation during droplet impact should increase the cell viability [69]. Another study modelled cell deformation during droplet impact in viscoelastic solutions [70]; it showed that for drop Weissenberg numbers $Wi_d = t_r \cdot V_{im}/d$ (where $V_{im}$ is the impact velocity and $d$ is the nozzle diameter) between 0.1 and 100, cell deformation decreased and therefore cell viability increased linearly with solution viscosity. In our experiments, Weissenberg numbers were 51 and 22 for 1% and 2% PVP, respectively. This is consistent with our observations that increasing the PVP concentration (and thus the solution viscosity) improves cell viability. The experimental results from this study showed that bioink viscosity (polymer concentration) plays a significant role in the average cell viability (%) of the printed cell-laden droplets.

The cell-laden droplets were printed directly into tissue-culture plates (8×8 array of droplets at 30 nL droplet volume per spot) using the optimal bioink (2% PVP, $3\times10^6$ cells/mL)

and cultured over a period of seven days to evaluate its proliferation profile. No negative control (nonprinted cells) was used for this study as the manual hand-held micropipettes can only dispense cell-laden droplets in the range of microliter (μL) volume and hence no fair comparison can be obtained between the printed and nonprinted cells. Only the printed groups (0% and 2% PVP-based bioinks at a constant cell concentration of $3\times10^6$ cells/mL) were used for comparison to understand the influence of PVP on cell proliferation over time. The PrestoBlue® assay was used for proliferative quantitative analysis in this study; the measured RFUs were directly proportional to the number of living cells, and all the measured values were normalized to Day 1 for easy comparison. The measured normalized RFUs over a period of seven days showed that the printed HDFs from both groups (0% and 2% PVP-based bioinks) continually proliferated (Fig. 4c), which confirmed that the encapsulated primary cells remained viable and retained their proliferative capability. Furthermore, the representative fluorescence images for both groups (Figs. 4d and 4e) showed that most of the printed HDFs showed elongated morphology at Day 1, and they proliferated well to reach almost about 80% confluency at Day 7.

### Cell patterning

The jetting-based bioprinting approach has a high degree of control over printed cell density by manipulating the number of printed cell-laden droplets at predefined positions. Hence, it is highly suitable for drop-on-demand precise patterning of multiple types of living cells and biomaterials to control the spatial arrangement of these functional components for various bioprinting applications [54, 71].

The HDFs were stained using green, orange, and blue cytoplasmic membrane dyes to simulate different types of cells and suspended in 2% PVP-based bioinks to obtain stained cells at a final concentration of $3\times10^6$ cells/mL. The printed cell density on a planar surface can be controlled by printing varying numbers of cell-laden droplets at each predefined location for cell patterning applications to achieve a cell density gradient across the planar substrate surface with lower cell density at the top left corner and higher cell density at the bottom right corner (Fig. 5a). Next, cell-laden PVP droplets stained with different dyes (green, orange, and blue) were printed using the thermal inkjet print-head directly into nonadherent 96-well round bottom plates filled with cell culture medium for fabrication of multicell spheroids (Fig. 5b). Although multicell spheroids can be fabricated easily using an inkjet-based bioprinting approach, it was noted that the printed number of blue-stained cells was lower than that of the green- and orange-stained cells even though the cell-laden PVP bioinks (green, orange, and blue) were dispensed at similar volumes. This was likely due to the difference in fluid properties (viscosity, surface tension and density) for various dyes, which led to lower dispensed volume and cell number for the blue-stained cells. Hence, volume calibration for different staining dyes should be performed to obtain the desired dispensed volume. Finally, the green- and orange-stained cells were printed at varying volume ratios (1:3, 1:2, 1:1, 2:1 and 3:1) using the thermal inkjet print-head directly into nonadherent 96-well round bottom plates filled with cell culture medium for fabrication of tunable cell spheroids (Fig. 5c). The use of 2% PVP-based bioink enabled the precise deposition of cell-laden droplets (in the nL range) at the bottom of the nonadherent 96-well round bottom plates that eventually fused together to form cell spheroids after 1 day of culture. Hence, the use of cell-laden 2% PVP-based bioink in an inkjet bioprinting system offered a simple approach to fabricate cell spheroids of varying sizes (nL range) using multiple cell types at a higher throughput than conventional manual pipetting approaches.

## Conclusions

The goal of this study showed that the bioink properties (bioink viscoelasticity and viscosity) have a huge influence on the printing performance and cell health in inkjet-based bioprinting. An inert polyvinylpyrrolidone (PVP360) polymer was used in this study to evaluate the printing performance—droplet formation (such as filament elongation, presence of satellite droplets and droplet displacement), droplet splashing and cell health (cell viability and proliferation). Our study showed that a higher bioink viscoelasticity helps to stabilize droplet filaments and create highly stretched polymer filaments, which induce the formation of highly aligned satellite droplets during the droplet pinch-off from the nozzle orifice. These satellite droplets from 2% PVP-based bioinks have a significantly higher percentage (71.4%) of total satellite droplets within 0.2 mm displacement compared to 0% (25.0%) and 1% (51.1%) PVP-based bioinks. Next, a significant increase in the bioink viscosity (2% PVP) facilitated droplet deposition on the wetted substrate surface in the absence of splashing and significantly improved the accuracy of deposited main droplets within 0.1 mm displacement to 90.0% compared to 1% (48.9%) and 1% (50.0%) PVP-based bioinks. Further analysis showed that cell-laden bioinks with higher viscosity exhibited higher measured average cell viability (%), as the presence of polymer within the printed droplets provides an additional cushioning effect (higher energy dissipation) for the encapsulated cells during droplet impact on the substrate surface, improves the measured average cell viability even at higher droplet impact velocity and retains the proliferation capability of the printed cells. Understanding the influence of bioink properties (e.g., bioink viscoelasticity and viscosity) on printing performance

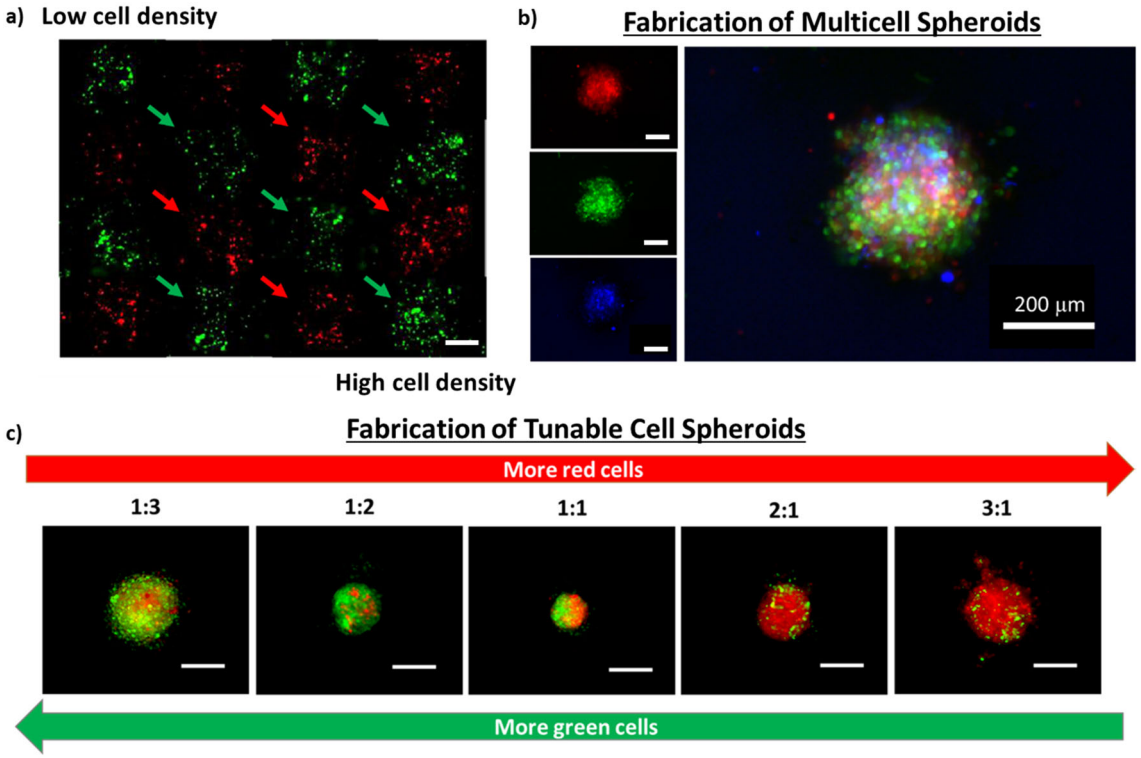


**Fig. 5** **a** Bioprinting of cell-laden droplets at predefined positions to manipulate printed cell density (low cell density at top left corner to high cell density at bottom right corner). **b** Fabrication of multicell spheroids using primary human fibroblasts stained with orange, green and blue cytoplasmic membrane dyes. **c** Fabrication of tunable cell spheroids at different volume ratios using primary human fibroblasts stained with orange and green cytoplasmic membrane dyes, scale bar=200 μm

and cell health is important for the formulation of new bioinks, and we have demonstrated precise DOD deposition of living cells and fabrication of tunable cell spheroids (nL–μL range) using multiple types of cells in a facile manner.

**Supplementary Information** The online version contains supplementary material available at https://doi.org/10.1007/s42242-023-00245-3.

**Acknowledgements** This study was supported under the RIE2020 Industry Alignment Fund—Industry Collaboration Projects (IAF-ICP) Funding Initiative, as well as cash and in-kind contribution from the industry partner, HP Inc., through the HP-NTU Digital Manufacturing Corporate Lab. We would also like to acknowledge and thank the D300e HP team for supplying the cell-dispensing cassettes for the experiments. Wei Long Ng would like to acknowledge support from NTU Presidential Postdoctoral Fellowship.

**Author contributions** WLN: conceptualization, methodology, investigation, visualization, writing—review & editing, and supervision. XH: investigation and writing.VS: investigation and writing. RS: investigation and visualization. WYY: funding acquisition and review.

## Declarations

**Conflict of interest** The authors declare that they have no conflict of interest.

**Ethical approval** This article does not contain any studies with human or animal subjects performed by any of the authors.

## References

1. Ng WL, Chua CK, Shen YF (2019) Print me an organ! why we are not there yet. Prog Polym Sci 97:101145. https://doi.org/10.1016/j.progpolymsci.2019.101145
2. Sun W, Starly B, Daly AC et al (2020) The bioprinting roadmap. Biofabrication 12(2):022002. https://doi.org/10.1088/1758-5090/ab5158
3. Levato R, Jungst T, Scheuring RG et al (2020) From shape to function: the next step in bioprinting. Adv Mater 32(12):1906423. https://doi.org/10.1002/adma.201906423
4. Ng WL, Chan A, Ong YS et al (2020) Deep learning for fabrication and maturation of 3D bioprinted tissues and organs. Virtual Phys Prototyp 15(3):340–358. https://doi.org/10.1080/17452759.2020.1771741
5. Lee JM, Ng WL, Yeong WY (2019) Resolution and shape in bioprinting: strategizing towards complex tissue and organ printing. Appl Phys Rev 6(1):011307. https://doi.org/10.1063/1.5053909
6. He JK, Mao M, Li X et al (2021) Bioprinting of 3D functional tissue constructs. Int J Bioprinting 7(3):1–2. https://doi.org/10.18063/ijb.v7i3.395
7. Ng WL, Wang S, Yeong WY et al (2016) Skin bioprinting: impending reality or fantasy? Trends Biotechnol 34(9):689–699. https://doi.org/10.1016/j.tibtech.2016.04.006

8. Guo F, Li P, French JB et al (2015) Controlling cell–cell interactions using surface acoustic waves. Proc Natl Acad Sci USA 112(1):43–48. https://doi.org/10.1073/pnas.1422068112
9. Ng WL, Yeong WY, Naing MW (2016) Microvalve bioprinting of cellular droplets with high resolution and consistency. In: Proceedings of the International Conference on Progress in Additive Manufacturing, pp 397–402
10. Choe YE, Kim GH (2020) A PCL/cellulose coil-shaped scaffold via a modified electrohydrodynamic jetting process. Virtual Phys Prototyp 15(4):403–416. https://doi.org/10.1080/17452759.2020.1808269
11. Kanaki Z, Chandrinou C, Orfanou IM et al (2022) Laser-induced forward transfer printing on microneedles for transdermal delivery of gemcitabine. Int J Bioprinting 8(2):554. https://doi.org/10.18063/ijb.v8i2.554
12. Ozbolat IT, Hospodiuk M (2016) Current advances and future perspectives in extrusion-based bioprinting. Biomaterials 76:321–343. https://doi.org/10.1016/j.biomaterials.2015.10.076
13. Zhuang P, Ng WL, An J et al (2019) Layer-by-layer ultraviolet assisted extrusion-based (UAE) bioprinting of hydrogel constructs with high aspect ratio for soft tissue engineering applications. PLoS One 14(6):e0216776. https://doi.org/10.1371/journal.pone.0216776
14. Ng WL, Yeong WY, Naing MW (2014) Potential of bioprinted films for skin tissue engineering. In: Proceedings of the 1st International Conference on Progress in Additive Manufacturing, pp 441–446. https://doi.org/10.3850/978-981-09-0446-3_065
15. Meng Z, He JK, Li JX et al (2020) Melt-based, solvent-free additive manufacturing of biodegradable polymeric scaffolds with designer microstructures for tailored mechanical/biological properties and clinical applications. Virtual Phys Prototyp 15(4):417–444. https://doi.org/10.1080/17452759.2020.1808937
16. Chand R, Muhire BS, Vijayavenkataraman S et al (2022) Computational fluid dynamics assessment of the effect of bioprinting parameters in extrusion bioprinting. Int J Bioprinting 8(2):545. https://doi.org/10.18063/ijb.v8i2.545
17. Ng WL, Lee JM, Zhou MM et al (2020) Vat polymerization-based bioprinting—process, materials, applications and regulatory challenges. Biofabrication 12(2):022001. https://doi.org/10.1088/1758-5090/ab6034
18. Li W, Mille LS, Robledo JA et al (2020) Recent advances in formulating and processing biomaterial inks for vat polymerization-based 3D printing. Adv Healthcare Mater 9(15):2000156. https://doi.org/10.1002/adhm.202000156
19. Nieto D, Marchal Corrales JA, de Mora AJ et al (2020) Fundamentals of light-cell–polymer interactions in photo-cross-linking based bioprinting. APL Bioeng 4(4):041502. https://doi.org/10.1063/5.0022693
20. Takagi D, Lin W, Matsumoto T et al (2019) High-precision three-dimensional inkjet technology for live cell bioprinting. Int J Bioprinting 5(2):208. https://doi.org/10.18063/ijb.v5i2.208
21. Xu T, Zhao WX, Zhu JM et al (2013) Complex heterogeneous tissue constructs containing multiple cell types prepared by inkjet printing technology. Biomaterials 34(1):130–139. https://doi.org/10.1016/j.biomaterials.2012.09.035
22. Gudupati H, Dey M, Ozbolat I et al (2016) A comprehensive review on droplet-based bioprinting: past, present and future. Biomaterials 102:20–42. https://doi.org/10.1016/j.biomaterials.2016.06.012
23. Ng WL, Zhi Qi JT, Yeong WY et al (2018) Proof-of-concept: 3D bioprinting of pigmented human skin constructs. Biofabrication 10(2):025005. https://doi.org/10.1088/1758-5090/aa9e1e
24. Agarwala S, Lee JM, Ng WL et al (2018) A novel 3D bioprinted flexible and biocompatible hydrogel bioelectronic platform. Biosens Bioelectron 102:365–371. https://doi.org/10.1016/j.bios.2017.11.039
25. Li X, Liu B, Pei B et al (2020) Inkjet bioprinting of biomaterials. Chem Rev 120(19):10793–10833. https://doi.org/10.1021/acs.chemrev.0c00008
26. Ng WL, Lee JM, Yeong WY et al (2017) Microvalve-based bioprinting—process, bio-inks and applications. Biomater Sci 5(4):632–647. https://doi.org/10.1039/C6BM00861E
27. Jentsch S, Nasehi R, Kuckelkorn C et al (2021) Multiscale 3D bioprinting by nozzle-free acoustic droplet ejection. Small Methods 5(6):2000971. https://doi.org/10.1002/smtd.202000971
28. Yusupov V, Churbanov S, Churbanova E et al (2020) Laser-induced forward transfer hydrogel printing: a defined route for highly controlled process. Int J Bioprinting 6(3):271. https://doi.org/10.18063/ijb.v6i3.271
29. Saunders RE, Derby B (2014) Inkjet printing biomaterials for tissue engineering: bioprinting. Int Mater Rev 59(8):430–448. https://doi.org/10.1179/1743280414Y.0000000040
30. Suntornnond R, Ng WL, Huang X et al (2022) Improving printability of hydrogel-based bio-inks for thermal inkjet bioprinting applications via saponification and heat treatment process. J Mater Chem B 10:5989–6000. https://doi.org/10.1039/D2TB00442A
31. Rastogi P, Kandasubramanian B (2019) Review of alginate-based hydrogel bioprinting for application in tissue engineering. Biofabrication 11(4):042001. https://doi.org/10.1088/1758-5090/ab331e
32. Xu C, Chai WX, Huang Y et al (2012) Scaffold-free inkjet printing of three-dimensional zigzag cellular tubes. Biotechnol Bioeng 109(12):3152–3160. https://doi.org/10.1002/bit.24591
33. Xu T, Catalin B, Michael A et al (2009) Fabrication and characterization of bio-engineered cardiac pseudo tissues. Biofabrication 1(3):035001. https://doi.org/10.1088/1758-5082/1/3/035001
34. Noor N, Shapira A, Edri R et al (2019) 3D printing of personalized thick and perfusable cardiac patches and hearts. Adv Sci 6(11):1900344. https://doi.org/10.1002/advs.201900344
35. Osidak EO, Kozhukhov VI, Osidak MS et al (2020) Collagen as bioink for bioprinting: a comprehensive review. Int J Bioprinting 6(3):270. https://doi.org/10.18063/ijb.v6i3.270
36. Lee JM, Suen SKQ, Ng WL et al (2020) Bioprinting of collagen: considerations, potentials, and applications. Macromol Biosci 21(1):2000280. https://doi.org/10.1002/mabi.202000280
37. Yang Y, Xu RZ, Wang CJ et al (2022) Recombinant human collagen-based bioinks for the 3D bioprinting of full-thickness human skin equivalent. Int J Bioprinting 8(4):611. https://doi.org/10.18063/ijb.v8i4.611
38. Nichol JW, Koshy ST, Bae H et al (2010) Cell-laden microengineered gelatin methacrylate hydrogels. Biomaterials 31(21):5536–5544. https://doi.org/10.1016/j.biomaterials.2010.03.064
39. Bertassoni LE, Cardoso JC, Manoharan V et al (2014) Direct-write bioprinting of cell-laden methacrylated gelatin hydrogels. Biofabrication 6(2):024105. https://doi.org/10.1088/1758-5082/6/2/024105
40. Ng WL, Yeong WY, Naing MW (2016) Development of polyelectrolyte chitosan-gelatin hydrogels for skin bioprinting. Procedia CIRP 49:105–112. https://doi.org/10.1016/j.procir.2015.09.002
41. Ng WL, Yeong WY, Naing MW (2016) Polyelectrolyte gelatin-chitosan hydrogel optimized for 3D bioprinting in skin tissue engineering. Int J Bioprinting 2(1):53–62. https://doi.org/10.18063/IJB.2016.01.009
42. Frisman I, Seliktar D, Bianco-Peled H (2011) Nanostructuring PEG-fibrinogen hydrogels to control cellular morphogenesis. Biomaterials 32(31):7839–7846. https://doi.org/10.1016/j.biomaterials.2011.06.078
43. Lee YB, Polio S, Lee W et al (2010) Bio-printing of collagen and VEGF-releasing fibrin gel scaffolds for neural stem cell culture. Exp Neurol 223(2):645–652. https://doi.org/10.1016/j.expneurol.2010.02.014

44. Gao G, Yonezawa T, Hubbell K et al (2015) Inkjet-bioprinted acrylated peptides and PEG hydrogel with human mesenchymal stem cells promote robust bone and cartilage formation with minimal printhead clogging. Biotechnol J 10(10):1568–1577. https://doi.org/10.1002/biot.201400635
45. Gao G, Schilling AF, Yonezawa T et al (2014) Bioactive nanoparticles stimulate bone tissue formation in bioprinted three-dimensional scaffold and human mesenchymal stem cells. Biotechnol J 9(10):1304–1311. https://doi.org/10.1002/biot.201400305
46. Gao G, Schilling AF, Hubbell K et al (2015) Improved properties of bone and cartilage tissue from 3D inkjet-bioprinted human mesenchymal stem cells by simultaneous deposition and photocrosslinking in PEG-GelMA. Biotechnol Lett 37(11):2349–2355. https://doi.org/10.1007/s10529-015-1921-2
47. Jang D, Kim D, Moon J (2009) Influence of fluid physical properties on ink-jet printability. Langmuir 25(5):2629–2635. https://doi.org/10.1021/la900059m
48. Zhang MY, Krishnamoorthy S, Song HT et al (2017) Ligament flow during drop-on-demand inkjet printing of bioink containing living cells. J Appl Phys 121(12):124904. https://doi.org/10.1063/1.4978744
49. Xu CX, Zhang M, Huang Y et al (2014) Study of droplet formation process during drop-on-demand inkjetting of living cell-laden bioink. Langmuir 30(30):9130–9138. https://doi.org/10.1021/la501430x
50. Blaeser A, Duarte Campos DF, Puster U et al (2016) Controlling shear stress in 3D bioprinting is a key factor to balance printing resolution and stem cell integrity. Adv Healthcare Mater 5(3):326–333. https://doi.org/10.1002/adhm.201500677
51. Shi J, Wu B, Li SH et al (2018) Shear stress analysis and its effects on cell viability and cell proliferation in drop-on-demand bioprinting. Biomed Phys Eng Express 4(4):045028. https://doi.org/10.1088/2057-1976/aac946
52. Luo Y, Hong YL, Shen L et al (2021) Multifunctional role of polyvinylpyrrolidone in pharmaceutical formulations. AAPS PharmSciTech 22:1–16. https://doi.org/10.1208/s12249-020-01909-4
53. Ng WL, Yeong WY, Naing MW (2017) Polyvinylpyrrolidone-based bio-ink improves cell viability and homogeneity during drop-on-demand printing. Materials 10(2):190. https://doi.org/10.3390/ma10020190
54. Ng WL, Ayi TC, Liu YC et al (2021) Fabrication and characterization of 3D bioprinted triple-layered human alveolar lung models. Int J Bioprinting 7(2):332. https://doi.org/10.18063/ijb.v7i2.332
55. Ng WL, Goh MH, Yeong WY et al (2018) Applying macromolecular crowding to 3D bioprinting: fabrication of 3D hierarchical porous collagen-based hydrogel constructs. Biomater Sci 6(3):562–574. https://doi.org/10.1039/C7BM01015J
56. Liu YY, Derby B (2019) Experimental study of the parameters for stable drop-on-demand inkjet performance. Phys Fluids 31(3):032004. https://doi.org/10.1063/1.5085868
57. Dong H, Carr WW, Morris JF (2006) An experimental study of drop-on-demand drop formation. Phys Fluids 18(7):072102. https://doi.org/10.1063/1.2217929
58. Meyer JD, Hewlett-Packard A, Bazilevsky A (1999) Effects of polymeric additives on thermal ink jets. Recent Prog Ink Jet Technol II:450–455
59. Kok CM, Rudin A (1981) Relationship between the hydrodynamic radius and the radius of gyration of a polymer in solution. Die Makromol Chem Rapid Commun 2(11):655–659. https://doi.org/10.1002/marc.1981.030021102
60. Xu DS, Sanchez-Romaguera V, Barbosa S et al (2007) Inkjet printing of polymer solutions and the role of chain entanglement. J Mater Chem 17(46):4902–4907. https://doi.org/10.1039/B710879F
61. Zhang YZ, Hu GF, Liu YH et al (2022) Suppression and utilization of satellite droplets for inkjet printing: a review. Processes 10(5):932. https://doi.org/10.3390/pr10050932
62. Josserand C, Thoroddsen ST (2016) Drop impact on a solid surface. Annu Rev Fluid Mech 48:365–391. https://doi.org/10.1146/annurev-fluid-122414-034401
63. Yarin AL (2006) Drop impact dynamics: splashing, spreading, receding, bouncing. Annu Rev Fluid Mech 38:159–192. https://doi.org/10.1146/annurev.fluid.38.050304.092144
64. Rioboo R, Tropea C, Marengo M (2001) Outcomes from a drop impact on solid surfaces. Atom Sprays. https://doi.org/10.1615/AtomizSpr.v11.i2.40
65. Mundo C, Sommerfeld M, Tropea C (1995) Droplet-wall collisions: experimental studies of the deformation and breakup process. Int J Multiph Flow 21(2):151–173. https://doi.org/10.1016/0301-9322(94)00069-V
66. Moreira ALN, Moita AS, Panão MR (2010) Advances and challenges in explaining fuel spray impingement: how much of single droplet impact research is useful? Prog Energy Combust Sci 36(5):554–580. https://doi.org/10.1016/j.pecs.2010.01.002
67. Wal RLV, Berger GM, Mozes SD (2006) The splash/non-splash boundary upon a dry surface and thin fluid film. Exp Fluids 40(1):53–59. https://doi.org/10.1007/s00348-005-0045-1
68. Ng WL, Huang X, Shkolnikov V et al (2022) Controlling droplet impact velocity and droplet volume: key factors to achieving high cell viability in sub-nanoliter droplet-based bioprinting. Int J Bioprinting 8(1):424. https://doi.org/10.18063/ijb.v8i1.424
69. Takamatsu H, Rubinsky B (1999) Viability of deformed cells. Cryobiology 39(3):243–251. https://doi.org/10.1006/cryo.1999.2207
70. Nooranidoost M, Izbassarov D, Tasoglu S et al (2019) A computational study of droplet-based bioprinting: effects of viscoelasticity. Phys Fluids 31(8):081901. https://doi.org/10.1063/1.5108824
71. Ng WL, Yeong WY (2019) The future of skin toxicology testing-3D bioprinting meets microfluidics. Int J Bioprinting 5(2.1):237. https://doi.org/10.18063/ijb.v5i2.1.237